

STL-free design and manufacturing paradigm for high-precision powder bed fusion

Junhao Ding^{a†}, Qiang Zou^{b†}, Shuo Qu^a, Paulo Bartolo^{(1)c}, Xu Song^{a*}, Charlie C. L. Wang^{c*}

^aDepartment of Mechanical and Automation Engineering, The Chinese University of Hong Kong, HKSAR, China

^bState Key Laboratory of CAD&CG, Zhejiang University, Hangzhou, China

^cDepartment of Mechanical, Aerospace and Civil Engineering, The University of Manchester, Manchester, UK

High-precision powder bed fusion (PBF), together with highly complex geometries necessitate a much more scalable representation of the geometry and an efficient computational pipeline. This paper presents a new digital design and manufacturing paradigm to solve the scalability and efficiency challenges by using the concept of STL-free workflow. It seamlessly integrates implicit solid modelling for design and direct slicing for manufacturing without any intermediate steps related to STL meshes. The presented paradigm has been validated by two case studies involving complex geometries filled with multiscale triply periodic minimal surfaces (TPMS), which are fabricated by PBF with laser beam size 25µm.

Additive manufacturing, Powder bed fusion, Implicit modelling, Direct slicing, Triply periodic minimal surfaces

1. Introduction

Additive manufacturing (AM) constructs 3D objects by accumulating materials, layer by layer [1]. This additive process was considered suitable only for prototype production, but nowadays it has been recognized as a valuable industrial-production technology due to the substantial improvement to precision and available material range [2]. In particular, the precision of laser-based powder bed fusion of metal (PBF-LB/M) has been increased to a level that it is possible to print metal parts with highly complex geometry and extremely fine details. This makes PBF-LB/M particularly suitable for producing lightweight lattice structures in high-performance.

Despite the abovementioned benefits, high-precision PBF-LB/M poses new challenges to the conventional digital pipeline of 3D printing, which first converts a given CAD model to a mesh representation in the Stereo Lithograph (STL) format, then slices the mesh to a series of planar contours, and finally generates toolpaths to fill those contours [3]. This STL-based pipeline is able to work satisfactorily for traditional PBF-LB/M and simple geometries where the number of a mesh's triangles is usually below 1M. However, the number of triangles becomes tremendously huge (e.g., 500M) when high-precision PBF-LB/M is used. Processing such a huge number of triangles would consume too much computer memory and time for the STL-based pipeline to run properly on a computer. The situation becomes even worse when the part to be printed has highly complex interior structures, e.g., triply periodic minimal surfaces (TPMS) [4,5]. For these reasons, a new computational pipeline is demanded to solve the efficiency challenge caused by processing highly complex structures for high-precision PBF-LB/M.

Most existing research works approach the above efficiency issue through improving the CAD-to-STL conversion procedure in the conventional 3D printing process pipeline [6]. The working principle is to minimize the number of triangles in meshing a CAD model, and Chougrani et al. [7] provide a typical example of that. Those methods can produce a notable reduction of triangles but have two serious limitations. First, different reduction ideas are developed for different CAD models, and no generic algorithm has been made available. Second, the developed algorithms still cannot

give sufficiently reduced triangles on models with freeform surfaces such as TPMS-based lattices.

There are also studies focusing on improving the STL-to-contour slicing procedure. This line of research appears to be initialized by Huang et al. [8], and is most recently improved by Feng et al. [9]. Instead of generating contours by triangle-plane intersections, they suggested the combined use of 3D distance fields and the marching square method. Nevertheless, no significant reduction of memory and time usage has yet been demonstrated, and this is not surprising since 3D distance fields require a massive amount of memory to store. The latest development [9] alleviated this issue by using analytical expressions to represent the 3D distance fields, but the primary focus was to slice open surfaces, not the solids considered in this work. In addition, only simple geometries (i.e., 1-level TPMS) and low-precision PBF-LB/M were studied. Although the ideas presented by Huang et al. [8] and Feng et al. [9] are promising, they have not offered a complete solution to the efficiency issue in both design and manufacturing.

In this paper, the efficiency issue is to be solved with the concept of STL-free, covering all aspects in design and manufacturing. As the issue is caused by the massive triangles in model representation, we propose to completely drop the use of meshes in the pipeline. Specifically, we seamlessly integrate the implicit solid modelling for design and the direct slicing for manufacturing. With implicit modelling, complex geometry can be efficiently modelled without any STL-related representation; with direct slicing, toolpaths can be directly generated from the implicit geometry without any intermediate steps related to STL meshes. Then, significant reduction of both memory and time consumption can be achieved. In our experiments, memory usage has been reduced to the level of 100MB, and the computing time is about 1s/slice in average, even for the complex 3-level TPMS-based lattices as shown in Fig. 7. This new digital paradigm of design and manufacturing will be presented in Section 2, with its validation given in Section 3. To make this presentation easy to understand, we will use the currently popular TPMS-based lattices as an example to walk through the process details. TPMS-based lattices need a tremendous number of triangles to be accurately represented due to the high surface area to volume ratio, and this provides a good example where the conventional process flow fails to work. It should, however, be noted that many lattice structures

[†] Equal contributions; * Corresponding authors.

have implicit representation schemes, e.g., the most commonly used strut-based lattices [10]. Design and manufacturing of these structures can all benefit from our work.

2. Digital Framework

The proposed digital framework consists of four steps (Fig. 1).

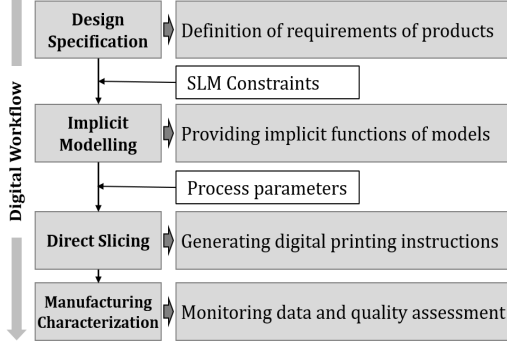


Fig. 1. Digital Framework

2.1. Design specification

This phase begins with an original product design idea which is subsequently converted to digital data, proving a definition of performance and functional requirements of product. Then, the internal structure, such as TPMS types, level of hierarchy, distribution of density, cell size and orientation are determined.

Although PBF-LB/M has the great benefits of design freedom, it does have limitations on manufacturability to be considered in this phase, which mainly comprise the following two aspects:

- Capability of the machine: The constraints include laser diameter, build envelop, limitation of data size, production time, clearance, roughness, and minimum feature size.
- Materials choice: The optimal processing parameters and requirements of the printing environment, such as energy absorption ratio, protecting gas, oxygen content, varies depending on the materials.

2.2. Implicit Modelling

Implicit three commonly applied P, G, D surfaces with intricate structures can be generated by the following functions [5]:

$$\begin{aligned}\phi_P(x, y, z) &= \cos(X) + \cos(Y) + \cos(Z) = C \\ \phi_G(x, y, z) &= \sin(X)\cos(Y) + \sin(Z)\cos(X) + \sin(y)\cos(Z) = C \\ \phi_D(x, y, z) &= \cos(X)\cos(Y)\cos(Z) - \sin(X)\sin(Y)\sin(Z) = C\end{aligned}$$

where $X = \frac{2\pi}{L}x$; $Y = \frac{2\pi}{L}y$; $Z = \frac{2\pi}{L}z$, C is a constant value controlling the interface surface, and L determines the cell size (see Fig. 2a). Taking G type TPMS sheet-network structure as an example, the solid sheet is enclosed by two surfaces with different constant C , rendered by Marching Cubes (MC) algorithm, as shown in Fig 2b.

Boolean operation can be efficiently applied between complex models based on implicit method as follows:

$$\begin{aligned}\text{Intersection: } \phi_{(A \cap B)}(x, y, z) &= \max(\phi_A(x, y, z), \phi_B(x, y, z)) \\ \text{Subtraction: } \phi_{(A - B)}(x, y, z) &= \max(\phi_A(x, y, z), -\phi_B(x, y, z)) \\ \text{Union: } \phi_{(A \cup B)}(x, y, z) &= \min(\phi_A(x, y, z), \phi_B(x, y, z))\end{aligned}$$

where $\phi_A(x, y, z)$ and $\phi_B(x, y, z)$ are implicit represented models. Solid zones, pore zones and surfaces of models are defined by the scalar value as: $\phi < 0$, $\phi > 0$, $\phi = 0$ respectively. The freeform external geometry of the G sheet can be obtained by the Boolean operations. For the solid in implicit representation, taking

the intersection as an example, a TPMS sheet with a sphere external boundary can be generated as shown in Fig. 2c. For mesh models, Boolean operations can be applied after converting them into an implicit representation such as distance field.

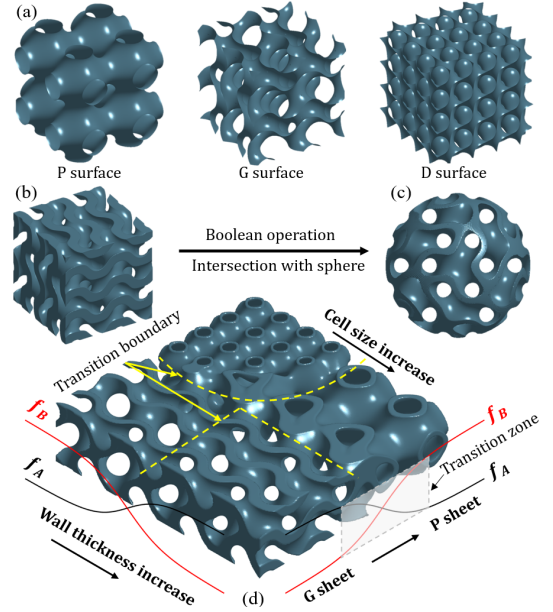


Fig. 2. TPMS of: (a) P, G, D type surfaces; (b) G sheet-network solid; (c) intersection with sphere; (d) graded structure

TPMS parameters, as well as types, cell size and wall thickness, can be efficiently controlled (e.g., the model shown in Fig. 2d). Here, the weighting functions, such as Sigmoid function, are employed to mix the various TPMS or other implicitly modelled structures with smooth transitions:

$$\phi(x, y, z) = f_A(x, y, z)\phi_A(x, y, z) + f_B(x, y, z)\phi_B(x, y, z)$$

where f_A and f_B are weighting functions. By controlling f_A and f_B , various transition zones and boundaries can be achieved, as shown in Fig. 2d.

Moreover, surface area, volume and wall thickness can be efficiently calculated according to the scalar value, which provides feedback to the implicit modelling design. Unlike mesh-based methods that are prone to robustness problems due to round-off errors, all these tools in our design pipeline are very robust.

2.3. Direct slicing

The high precision of PBF-LB/M and the high surface area to volume ratio in TPMS require for a direct slicing method without any intermediate steps of triangular mesh construction and processing. Our method consists of three steps: (1) point membership classification for a slicing plane, see Fig. 3b; (2) contour extraction from the classified plane, refer to Fig. 3c; and (3) toolpath generation based on the extracted contours, see Fig. 3d.

The method classifies any points on every slicing plane as either IN-Solid or OUT-Solid. By IN-Solid we mean a point is within the solid of the TPMS, and OUT-Solid if otherwise. Specifically, a point (x_0, y_0, z_0) is IN-Solid if $\phi(x_0, y_0, z_0) \leq 0$, and OUT-Solid if $\phi(x_0, y_0, z_0) > 0$. With point membership classified for a given slicing plane, its contours emerge immediately as the boundary between planar regions occupied by IN-Solid and those by OUT-Solid. Algorithmically, this boundary can be attained by using the marching square method [8], which grows sampled points in between IN-Solid and OUT-Solid to be edge loops (i.e., contours). The extracted contours are stored in the CLI format [11]. Having

obtained the CLI file, toolpaths and their associated G-code can be readily generated using commercial software.

The above direct method reduces the dimension of the slicing problem from 3D to 2D, and thus all the memory consumption related to the building direction can be saved. Approximately, memory usage can be reduced at least by times of the number of layers, as will be shown in the case study. It can also significantly decrease slicing time since the time-consuming procedures of triangle mesh reconstruction and processing are completely avoided.

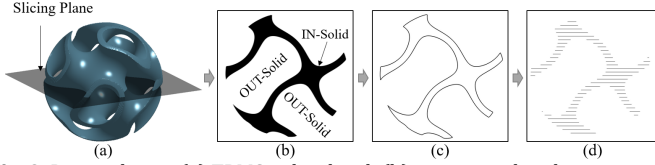


Fig. 3. Direct slicing: (a) TPMS to be sliced; (b) point membership classification; (c) contour extraction; and (d) toolpath generation.

2.4. Manufacturing and Characterization

Subsequently, the process parameters, such as laser powder, scanning speed, hatch distance are determined. Moreover, several scanning strategies have been developed to minimize the thermal stress in each layer of part so as to eliminate part distortion, including meander, stripe, and chessboard scanning modes.

Morphology, dimensional accuracy and surface roughness can be inspected by Optical microscope, Coordinate Measure Machine and 3D laser Scanning Microscope. The volumetric data and internal defects size and distribution can be obtained by micro-CT, if needed.

3. Case study

In this section, a case to design and fabricate a multiscale TPMS sheet and bone scaffold with high surface area to volume ratio and low relative density are presented to illustrate how proposed method is implemented with the PBF-LB/M process.

3.1. Design Specification and modelling

The experiment was conducted using SS316L stainless steel powder with size range 5~23 μ m and D50=15 μ m. A modified Han's Laser M100 machine using a 500W IPG fibre laser with a beam diameter of 25 μ m, was employed to print the design structures.

Table 1

Implicit model parameters

Multiscale TPMS	1-level	2-level	3-level
Cell size (mm)	24	6	1.5
Constant C	+/- 0.7	+/- 0.7	+/- 0.5
Relative density (%)	45.0	20.4	10.3
Surface area to volume ratio (%)	0.8	2.7	15.2

Fig.4 shows how the multiscale TPMS sheet in 3 levels with the relative density as 10.3% is generated by implicit modelling methodology. The modelling parameters are summarized in Table 1. The 1-level G sheet, with an external shape of the cube, is generated by enclosing the two G surfaces with different C constants. Consequently, the space is divided into 3 regions: Domain A, Domain B and Sheet as shown in Fig. 4d, and this separation phenomenon also exists in other level G sheets. Then, the 2-level G sheet is obtained by the subtraction of 2-level Domain A and B from 1-level sheet, as illustrated in Fig. 4e. The same relation is applied to generate the 3-level G sheet. 2D-Slicing confirmed that the high-level G sheet was generated in the low-level G sheet region, which guarantees the connectivity of TPMS

structure. More importantly, the multiscale TPMS in more levels can be obtained by applying this method iteratively. As shown in Table 1, applying hierarchical structure enables achieving better properties of the design, i.e. the surface area to volume ratio of 3-level multiscale TPMS is 15.2. By contrast, the surface to volume ratio of 1-level TPMS is only 0.8.

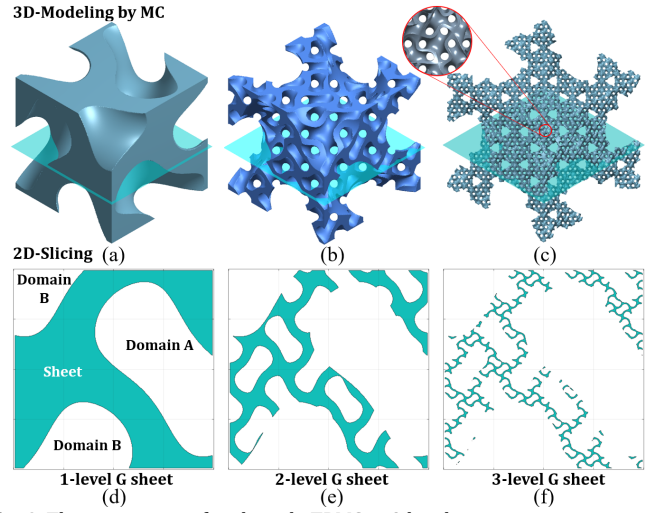


Fig. 4. The generation of multiscale TPMS in 3 levels.

Based on the aforementioned modelling method, a bone scaffold filled with multiscale G sheet in 3 levels is constructed by applying Boolean operation. The cell size of 1-level, 2-level and 3-level are 12mm, 3mm and 0.75mm respectively and the wall thickness is 65 μ m, as shown in Fig. 5.

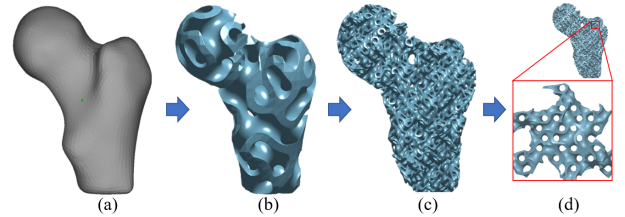


Fig. 5. Bone scaffold: (a) Primary bone; (b) 1-level; (c) 2-level; (d) 3-level

3.2. Slicing and Process building

The direct slicing method presented in Section 2.3 has been successfully applied to the cube model in Fig. 4c and the bone model in Fig. 5d. Their size information can be found in the second column of Table 2. To accommodate our high-precision PBF-LB/M (with beam diameter 25 μ m), the slicing resolution is set as 0.02mm (x-direction) * 0.02mm (y-direction) * 0.01mm (z-direction). If using the conventional 3D printing pipeline, it fails to work due to the high memory and processing time derived by such a dense resolution. Take the cube model as an example, the traditional marching cubes method would need 16 GB memory to run properly, and the resulting triangle mesh has approximately 282.8 million faces and 141.4 million vertices, which in turn requires 26.7 GB memory (using the half-edge data structure) to perform mesh processing. By contrast, our method only took a peak memory of 87.3MB; in terms of computing time, the method only took 0.73s/slice, using a 3.0GHz Intel I7-9700 Core with 16GB Memory. The bone model renders a much harder case; nevertheless, our method managed to handle it with a slightly higher cost of peak memory 108.9MB and average time 1.13s/slice. This demonstrates that our method has a very good scalability with the model's sizes as well as complexity.

Table 2 Slicing statistics of the tested models

Model	Size ($x * y * z$ mm)	Resolution ($\Delta x * \Delta y * \Delta z$ mm)	Peak memory (Mb)	Time (s/slice)
TPMS	20 * 20 * 20	0.02 * 0.02 * 0.01	87.3	0.73
Bone	31.5 * 21 * 42.5	0.02 * 0.02 * 0.01	108.9	1.13

Note: used a 3.0GHz Intel I7-9700 Core with 16GB Memory

Having attained the contours (stored as a CLI file) at each slicing plane, the commercial software HansMpath was used to generate the G-code job to drive our PBF-LB/M. The process parameters employed for the print were given in Table 3. A common scanning strategy, rotating the scan pattern for each successive layer by 67 degrees, was used to reduce residual stresses.

Table 3
 μ PBF -LB/M Process parameters

Laser power	Scanning speed	Layer thickness	Hatch distance
50 W	1000 mm/s	10 μ m	50 μ m

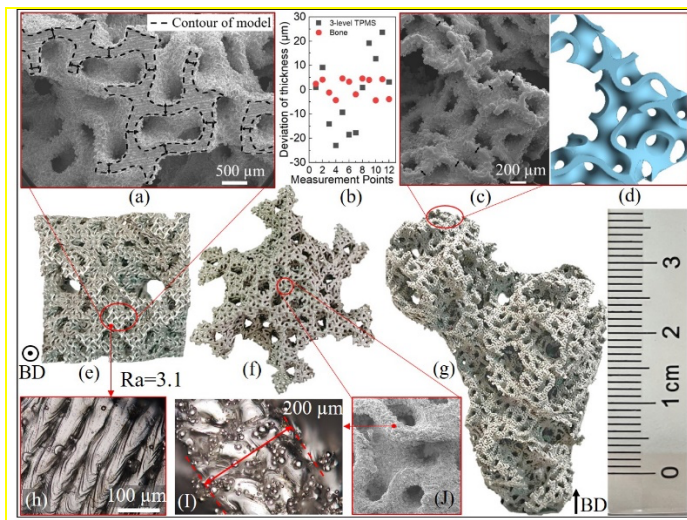


Fig. 6. Photographs, microstructure and thickness deviations of multiscale TPMS and bone scaffold

3.3. Manufacturing and Characterization

The multiscale TPMS in 3 levels and bone scaffold were printed as shown in Fig. 6. The wall thickness and roughness of TPMS were investigated by the optical microscope, showing that high printing accuracy (to the design specification) and low roughness ($R_a \sim 3\mu\text{m}$) can be achieved comparing to the conventional PBF process.

As shown in Fig.6a, the contour of the designed model is presented by dash lines and compared with the cross-section of the actual printed model under SEM. It demonstrates that the printed area is quite consistent with the designed model. Moreover, the comparison between actual print (Fig. 6c) and digital model (Fig. 6d) of bone scaffold shows that the fine details can also be printed accurately. The thickness deviations of 3-level TPMS and bone scaffold are in the range of $-25\mu\text{m}$ to $25\mu\text{m}$ and $-5\mu\text{m}$ to $5\mu\text{m}$, respectively (Fig. 6b). Such difference is believed to be caused by the scanning process. For large cross-sections, as the printed thickness is always the integral multiple of hatch distance, whether outer skin layer is scanned or not will lead to great difference. On the other hand, for small cross-sections when the wall thickness is below $60\mu\text{m}$, only single track is planned/printed. This results in a constant wall thickness, which is irrespective of designed value, but mainly determined by the melting pool size and the laser spot size.

Three passive cooling tests were also repeatedly conducted to demonstrate the effect of the surface-to-volume ratio of different

TPMS designs. A FLIR A655sc infrared camera was used to capture temperature. The hollowed 1-level TPMS and 3-level multiscale TPMS have weights as 5.6g and 6.9g, respectively. The TPMS in 3 levels with larger surface area to volume ratio thus achieves a remarkable higher cooling rate, as shown in Fig 7. This provides additional evidence for the advantages of having multi-level TPMS design and its associated manufacturing method, which has potential for high-performance thermal management devices such as heat exchangers and heat sinks in the future.

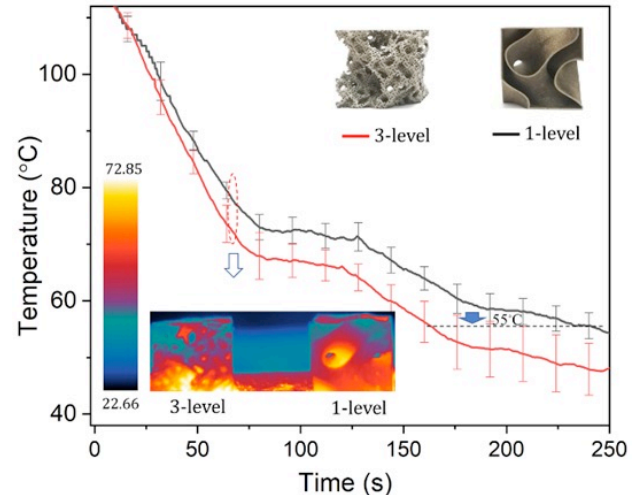


Fig. 7. Passive cooling test temperature history and cooling time (from 110°C to 55°C): 1-level: 249s, 3-level:167s

4. Conclusions

By our implicit modelling methodology and direct slicing pipeline, ultra-complex multiscale TPMS in 3 levels and bone scaffold can be modelled and fabricated with high accuracy and low memory cost. The experiments show that this new computational pipeline is good at processing complex models and the multiscale TPMS provides a way to improve surface area to volume ratio, achieving high performance and lightweight. We plan to conduct more research work in the future to exploit the applications of using multi-types, different sizes, density and orientations in graded TPMS structures.

References

- [1] Schmidt M, Merklein M, Bourell D, Dimitrov D, Hausotte T, Wegener K, Overmeyer L, Vollertsen F, Levy G N (2017) Laser based additive manufacturing in industry and academia. CIRP Annals 66(2): 561-583.
- [2] Bourell D, Kruth J P, Leu M, Levy G, Rosen D, Beese A M, Clare A (2017) Materials for additive manufacturing. CIRP Annals 66(2): 659-681.
- [3] Thompson M K, Moroni G, Vaneker T, Fadel G, Campbell R I, Gibson I, Bernard A, Schulz J, Graf P, Ahuja B, Martina F (2016). Design for Additive Manufacturing: Trends, opportunities, considerations, and constraints. CIRP Annals 65(2): 737-760.
- [4] Vaneker T, Bernard A, Moroni G, Gibson I, Zhang Y (2020) Design for additive manufacturing: Framework and methodology. CIRP Annals 69(2): 578-599.
- [5] Yoo D J (2014). Advanced projection image generation algorithm for fabrication of a tissue scaffold using volumetric distance field. International journal of precision engineering and manufacturing 15(10): 2117-2126.
- [6] Wu Y, Gupta A, Kurzeja K, Rossignac J (2020) Choccc: Convex hull of cospherical circles and applications to lattices. Computer-Aided Design 129:102903.
- [7] Chougrani L, Pernet J P, Veron P, Abed S (2017) Lattice structure lightweight triangulation for additive manufacturing. Computer-Aided Design 90: 95-104.
- [8] Huang P, Wang C C L, Chen Y (2013) Intersection-free and topologically faithful slicing of implicit solid. Journal of Computing and Information Science in Engineering, 13(2): 021009.
- [9] Feng J, Fu J, Lin Z, Shang C, Niu X (2019) Layered infill area generation from triply periodic minimal surfaces for additive manufacturing. Computer-Aided Design 107: 50-63.
- [10] Tang Y, Xiong Y, Boddeti, G N, Rosen D W (2019) Generation of Lattice Structures with Convolution Surface. CAD conference, Singapore, 69-74.
- [11] Zhang Z, Joshi S (2017) Slice data representation and format for multi-material objects for additive manufacturing processes. Rapid Prototyping Journal 23(1): 149-161.